Research Article Vol. 16, No. 2 / 1 Feb 2025 / Biomedical Optics Express 837
Biomedical Optics EXPRESS

Multi-modal transport of intensity diffraction tomography microscopy with an electrically tunable lens [Invited]

ZIHAO ZHOU,[1,2,3,†] RUNNAN ZHANG,[1,2,3,†] NING ZHOU,[1,2,3] QIAN CHEN,[3] AND CHAO ZUO[1,2,3,*]

[1]*Smart Computational Imaging Laboratory (SCILab), School of Electronic and Optical Engineering, Nanjing University of Science and Technology, Nanjing, Jiangsu 210094, China*
[2]*Smart Computational Imaging Research Institute (SCIRI) of Nanjing University of Science and Technology, Nanjing, Jiangsu 210019, China*
[3]*Jiangsu Key Laboratory of Spectral Imaging & Intelligent Sense, Nanjing University of Science and Technology, Nanjing, Jiangsu 210094, China*
[†]The authors contributed equally to this work.
[*]*zuochao@njust.edu.cn*

Abstract: Optical diffraction tomography (ODT) is an important technique for three-dimensional (3D) imaging of semi-transparent biological samples, enabling volumetric visualization of living cells, cultures, and tissues without the need for exogenous dyes. However, ODT faces significant challenges in imaging complex biological specimens due to the limited specificity of refractive index (RI) and the coupled relationship between absorption and phase in image formation. Here, we present multi-modal transport of intensity diffraction tomography (MM-TIDT), a high-speed 3D microscopy technique that integrates an electrically tunable lens with modified illumination patterns to decouple phase and absorption information. Leveraging dual illumination schemes–circular and annular apertures–MM-TIDT acquires two intensity stacks, facilitating accurate phase and absorption decoupling. Based on an alternating direction method of multipliers (ADMM) framework with total variation (TV) and non-negativity regularization, our method reconstructs multi-modal 3D distributions of fluorescence and complex RI with high accuracy and robustness. Experimental validation with fluorescent polystyrene microspheres, Spirulina specimens, and DAPI-labeled C166 cells demonstrates the multi-modal imaging capability of MM-TIDT to resolve fine structural details across diverse sample types, providing a versatile platform for exploring dynamic biological processes and intricate cellular interactions.

1. Introduction

In the field of biomedical imaging, researchers have long sought more efficient and non-destructive imaging techniques to reveal the intricate microscopic structures and dynamic processes within biological samples. Conventional imaging methodologies, which frequently depend on exogenous substances such as fluorescent labels or radioactive isotopes, pose not only the potential for sample damage but also result in complex protocols and substantial outlay [1–5]. Against this backdrop, quantitative phase imaging (QPI) [6–9], a label-free imaging technique that utilizes refractive index (RI) to image biological samples, has gained significant attention as a prospective approach for cellular and tissue imaging. By leveraging the phase information of transmitted light, which reflects the RI and morphological characteristics of the sample, QPI enables imaging of weakly absorbing samples without the need for fluorescent staining, thus avoiding the adverse effects of exogenous dyes. However, imaging based on refractive index lacks specificity compared to fluorescence microscopy. Furthermore, the limitation of two-dimensional (2D) imaging in QPI becomes particularly evident when dealing with biological samples with complex structures. It can only provide the axial projection of the three-dimensional (3D) structure on a 2D plane

#545258 https://doi.org/10.1364/BOE.545258
Journal © 2025 Received 15 Oct 2024; revised 20 Dec 2024; accepted 7 Jan 2025; published 31 Jan 2025

Biomedical Optics EXPRESS

[10], which is insufficient for representing the complete internal structural features of the sample, hindering further research. Therefore, developing 3D microscopy techniques capable of characterizing the internal structures of complex samples is of great significance. Among these, optical diffraction tomography (ODT) [11–16], a 3D RI tomography technique, is emerging as a key force driving innovation in 3D imaging technologies.

Classical ODT techniques, particularly holographic tomography, generally necessitate the employment of coherent light sources, scanning devices, or sample rotation stages to capture 2D holograms that encode both phase and amplitude information of the sample [17–22]. Over the past decade, although interferometric methods have witnessed tremendous progress, the use of coherent illumination inevitably introduces speckle noise, which can significantly degrade image quality. Furthermore, the necessity for rotation and scanning devices complicates the system, limiting its integration potential with other multi-modal microscopy systems.

Compared to the challenges posed by interferometric methods, non-interferometric approaches, such as phase retrieval techniques, offer significant advantages in terms of system simplicity, integration, and signal-to-noise ratio. One such technique, Fourier ptychographic diffraction tomography (FPDT) [23,24], iteratively reconstructs 3D, large-field, high-resolution RI information using a series of multi-angle illumination (including high-angle dark-field illuminations beyond the NA of the objective) intensity images. However, this technique is inevitably accompanied by lower imaging efficiency, complex computational processes, and difficulty in reconstructing thick samples. In contrast to iterative methods, intensity diffraction tomography (IDT) [25,26], a linear solution approach, employs a linear forward model to solve for the 3D RI distribution directly from intensity measurements by using the slice transfer function of a 3D sample under different illumination angles. This offers a low computational cost imaging solution for weakly scattering samples. However, these techniques typically scan illumination angles on a single focal plane, limiting their application to thick samples. Transport of intensity diffraction tomography (TIDT) [14,16] extends transport of intensity equation (TIE) [8,27,28], a 2D intensity-based QPI technique into a 3D RI diffraction tomography method. By performing axial scanning, the 3D intensity images can be represented as the linear superposition of the absorption and phase components of the scattering potential convolved with the corresponding absorption and phase point spread functions. TIDT avoids the complex computational steps and provides high-resolution, label-free 3D imaging for thick samples. Its simple system design, low cost, and ease of integration with existing microscopy systems make it a promising solution.

The TIDT technique is capable of reconstructing the 3D refractive index distribution of purely phase (or weakly absorption) objects using a single intensity stack, followed by deconvolution with the transfer function. However, for complex samples containing both absorption and phase components, the information from these two parts is coupled within a single scanning stack, making it difficult to simultaneously recover both through a single linear deconvolution. One way is to assume the phase-attenuation duality [29,30], similar to 2D phase imaging, where the phase and absorption are linearly related. However, this method has limited universality. Another approach employs focus scanning to eliminate phase information, thereby decoupling absorption information across a broader depth of field [31], while this method is limited to capturing 2D absorption data. Alternatively, multiple scanning stacks containing coupled information can be used to reconstruct both refractive index and absorption components, but this method typically requires the acquisition of several stacks [32]. Bai's work [33] decoupled the phase and absorption components of complex refractive index in the TIDT microscopy using only two intensity stacks under partially coherent illuminations. Compared to previous work, we employed an incoherent circular illumination, matched to the numerical aperture (NA) of the objective, to capture pure absorption information, and a partially coherent annular illumination, tangent to the NA, to acquire the coupled information. The reconstruction was iteratively optimized using the Alternating Direction Method of Multipliers (ADMM) [34] combined with total variation

Biomedical Optics EXPRESS

(TV) regularization [35] and non-negative prior. The advantages of our method are as follows: (1) By utilizing the pure absorption stack with an incoherent illumination pattern, the system resolution can reach the incoherent diffraction limit; (2) The TV algorithm implemented with the ADMM method effectively produces more reliable convergence results, particularly in terms of edge preservation; (3) The missing-cone problem, which results in a poor axial resolution several times worse than the lateral one and seriously impedes the reconstruction accuracy of the RI values, was relieved according to TV regularization and non-negative prior. Additionally, we incorporated a $4f$ telecentric system with an electrically tunable lens located at the Fourier plane after the native microscopy imaging system, aiming to replace the mechanical axial scanning with the high-speed instrument. This optimized the stack acquisition speed while minimizing errors caused by mechanical motion. Our algorithm has also been validated for wide-field fluorescence imaging, reducing the impact of out-of-focus stray fluorescence and enhancing the system's multi-modal imaging capability [31,36,37]. We initiated our experimental validation with a standard specimen, fluorescent microspheres, to verify the effectiveness of the MM-TIDT method, the results of which were in concordance with the simulations. We further demonstrated its utilities for different specimens such as Spirulina specimen and C166 cells, revealing the developed MM-TIDT method is a promising tool for broad applicability in the study of biological imaging.

2. Principle and methods

2.1. Forward imaging model of TIDT under partially coherent illumination

When light passes through a sample, the interaction between the light waves and the internal structures produces a complex scattered field. To simplify the analysis of this scattering process, various approximation methods have been applied. Among them, the first-order Born approximation [38] assumes that the incident light undergoes only a single scattering event and that the scattered field does not interact further with the sample. This approximation is widely applicable for weakly scattering samples. In contrast, the Rytov approximation [39] can handle multiple scattering events, though it introduces more complex computations. Since the scattering potential of an object contains detailed information about the complex RI of thick samples, Wolf [38], under the first-order Born approximation, provided a method for reconstructing the complex RI from the scattering potential:

$$f(\mathbf{r}) = k_0^2\left[n_0^2 - n^2(\mathbf{r})\right] \tag{1}$$

where $\mathbf{r} = (x, y, z)$ represents the 3D spatial domain coordinates, $k_0 = 2\pi/\lambda$ is the wavenumber, and λ is the wavelength. The parameter n_0 denotes the RI of the surrounding medium, while $n = n_{\mathrm{Re}} + \mathrm{i}\cdot \mathrm{n}_{\mathrm{Im}}$ is the complex RI of the sample. The real part of the complex RI, n_{Re}, represents the phase delay experienced by light passing through the sample, corresponding to the phase component of the sample. The imaginary part, n_{Im}, represents the absorption component of the sample. Similarly, the real part of the complex scattering potential, f_{Re}, corresponds to the phase component of the sample, while the imaginary part, f_{Im}, corresponds to the absorption component.

Under the first-order Born approximation, Streibl [40] derived a linear relationship between the scattering potential spectrum, $\widetilde{F}$, and the spectrum of the recorded image intensity, $\widetilde{I}$:

$$\widetilde{I}(\mathbf{u}) = B_0\delta(\mathbf{u}) + \widetilde{f}_{\mathrm{Re}}(\mathbf{u})H_P(\mathbf{u}) + \widetilde{f}_{\mathrm{Im}}(\mathbf{u})H_A(\mathbf{u}) \tag{2}$$

where $\mathbf{u}$ represents 3D frequency domain coordinates, and $B_0\delta(\mathbf{u})$ corresponds to the DC component transmitted by the system, representing the background intensity. The terms H_P and H_A are the system's phase absorption transfer function, respectively. From Eq. (2), it can be found that the spectrum of the acquired image intensity is the product of the real and imaginary

Biomedical Optics EXPRESS

parts of the sample's scattering potential with the corresponding optical transfer functions (OTF) of the system. The system's OTFs depend on factors such as the light source, aperture, and system parameters. We can express the aperture function of the circular objective lens, $P(\boldsymbol{\mu})$, as:

$$P(\boldsymbol{\mu}) = \begin{cases} 1, & |\boldsymbol{\mu}| \le \rho_p \\ 0, & |\boldsymbol{\mu}| > \rho_p \end{cases} \tag{3}$$

where $\boldsymbol{\mu}$ represents the lateral spatial fre quency coordinate corresponding to x and y, and ρ_p is the normalized frequency corresponding to the NA of the objective lens. For the light source function $S(\boldsymbol{\mu})$, a circular light source with a size comparable to the objective's NA, and an annular light source with an outer radius equivalent to the objective's NA, can be expressed as follows:

$$\begin{aligned} S(\boldsymbol{\mu})_{\text{Circular}} &= \begin{cases} 1, & |\boldsymbol{\mu}| \le \rho_p \\ 0, & |\boldsymbol{\mu}| > \rho_p \end{cases} \\ S(\boldsymbol{\mu})_{\text{Annular}} &= \begin{cases} 1, & \rho_p' \le |\boldsymbol{\mu}| \le \rho_p \\ 0, & \text{other} \end{cases} \end{aligned} \tag{4}$$

Building on Streibl's work [40–42], the analytic expressions for absorption transfer function and phase transfer function under non-paraxial conditions can be derived as follows [8,43]:

$$\begin{aligned} H_A(\boldsymbol{\mu},\eta) &= \frac{\lambda}{4\pi}\iint P\left(\boldsymbol{\mu}'+\frac{\boldsymbol{\mu}}{2}\right)P^*\left(\boldsymbol{\mu}'-\frac{\boldsymbol{\mu}}{2}\right)\times\left[S\left(\boldsymbol{\mu}'+\frac{\boldsymbol{\mu}}{2}\right)+S\left(\boldsymbol{\mu}'-\frac{\boldsymbol{\mu}}{2}\right)\right] \\ &\quad\times\delta\left[\eta+\sqrt{\lambda^{-2}-\left(\boldsymbol{\mu}'+\frac{\boldsymbol{\mu}}{2}\right)^2}-\sqrt{\lambda^{-2}-\left(\boldsymbol{\mu}'-\frac{\boldsymbol{\mu}}{2}\right)^2}\right]\mathrm{d}^2\boldsymbol{\mu}' \\ H_P(\boldsymbol{\mu},\eta) &= \frac{\mathrm{i}\lambda}{4\pi}\iint P\left(\boldsymbol{\mu}'+\frac{\boldsymbol{\mu}}{2}\right)P^*\left(\boldsymbol{\mu}'-\frac{\boldsymbol{\mu}}{2}\right)\times\left[S\left(\boldsymbol{\mu}'+\frac{\boldsymbol{\mu}}{2}\right)-S\left(\boldsymbol{\mu}'-\frac{\boldsymbol{\mu}}{2}\right)\right] \\ &\quad\times\delta\left[\eta+\sqrt{\lambda^{-2}-\left(\boldsymbol{\mu}'+\frac{\boldsymbol{\mu}}{2}\right)^2}-\sqrt{\lambda^{-2}-\left(\boldsymbol{\mu}'-\frac{\boldsymbol{\mu}}{2}\right)^2}\right]\mathrm{d}^2\boldsymbol{\mu}' \end{aligned} \tag{5}$$

where η represents the axial spatial frequency coordinate. By substituting the Eq. (3) and Eq. (4) into the Eq. (5), the 3D absorption transfer function and the 3D phase transfer function can be obtained under the specified illumination aperture, establishing the forward imaging model for the system.

2.2. Inverse reconstruction method for TIDT phase and absorption decoupling

As shown in Eq. (2), the intensity spectrum of the directly acquired images contains both the absorption and phase components of the scattering potential spectrum and these two components are coupled. To decouple them, we use the method of capturing image stacks under two different illumination apertures. After capturing two sets of stacks using two different illumination apertures, background removal and normalization are performed on the images. Then, by incorporating them into Eq. (2), the problem is transformed into solving a system of linear equations, with the objective function represented as:

$$\min \sum_t \left\| \tilde{I}_t - H_{P,t}\cdot\tilde{f}_{\text{Re}} - H_{A,t}\cdot\tilde{f}_{\text{Im}} \right\|_2^2 + \alpha\left\|\tilde{f}_{\text{Re}}\right\|_2^2 + \beta\left\|\tilde{f}_{\text{Im}}\right\|_2^2 \tag{6}$$

where $\widetilde{I}_t$ represents the Fourier transform of the actually acquired stack, and $T\widetilde{f}$ is the predicted spectral measurement based on the current estimate and the forward model. The variable t

Biomedical Optics EXPRESS

denotes the number of illumination apertures, while α and β are the regularization parameters corresponding to $\widetilde{f}_{\mathrm{Re}}$ and $\widetilde{f}_{\mathrm{Im}}$. Letting the derivatives of $\widetilde{f}_{\mathrm{Re}}$ and $\widetilde{f}_{\mathrm{Im}}$ in the objective function be zero respectively, yields:

$$\begin{aligned} f_{\mathrm{Re}} &= \mathcal{F}^{-1}\left\{A\left[\left(\sum_t |H_{A,t}|^2+\beta\right)\cdot\left(\sum_t H^*_{P,t}\cdot\tilde{I}_t\right)-\left(\sum_t H^*_{P,t}\cdot H_{A,t}\right)\cdot\left(\sum_t H^*_{A,t}\cdot\tilde{I}_t\right)\right]\right\} \\ f_{\mathrm{Im}} &= \mathcal{F}^{-1}\left\{A\left[\left(\sum_t |H_{P,t}|^2+\alpha\right)\cdot\left(\sum_t H^*_{A,t}\cdot\tilde{I}_t\right)-\left(\sum_t H_{P,t}\cdot H^*_{A,t}\right)\cdot\left(\sum_t H^*_{P,t}\cdot\tilde{I}_t\right)\right]\right\} \end{aligned} \tag{7}$$

where $\mathcal{F}^{-1}$ is the inverse 2D Fourier transform and A is the normalization term, which is specified as $A = 1/[(\Sigma_t|H_{P,t}|^2+\alpha)\cdot(\Sigma_t|H_{A,t}|^2+\beta)-(\Sigma_t H_{P,t}\cdot H^*_{A,t})\cdot(\Sigma_t H^*_{P,t}\cdot H_{A,t})]$. After obtaining the scattering potential, Eq. (1) is used to solve for the 3D distribution of RI and absorption components.

Due to the missing cone problem in the 3D OTF, artifacts often affect RI reconstruction. To address this, we employ TV regularization and non-negativity constraints as prior conditions. TV regularization minimizes the total variation of the image gradient, smoothing the results while preserving edges and fine details in the image. The application of the ADMM algorithm (See Supplement 1 S1 for details) allows for alternating optimization of the data fitting term and the TV regularization term, avoiding the difficulty of directly optimizing complex data. Additionally, since the RI of the medium used in the experiment is slightly smaller than that of the sample, we apply non-negativity constraints on the reconstructed RI to further improve the results.

2.3. TIDT platform combined with a high-speed electrically tunable lens

The experimental setup is based on a commercial inverted microscope (Zeiss Observer Z1) equipped with a 40 ×, 0.6 NA OLYMPUS objective. Illumination is provided by a programmable LED array (64 × 64, 0.5 mm spacing) that delivers quasi-monochromatic light. This array has been modified and installed at the original microscope light source location, 70 mm from the

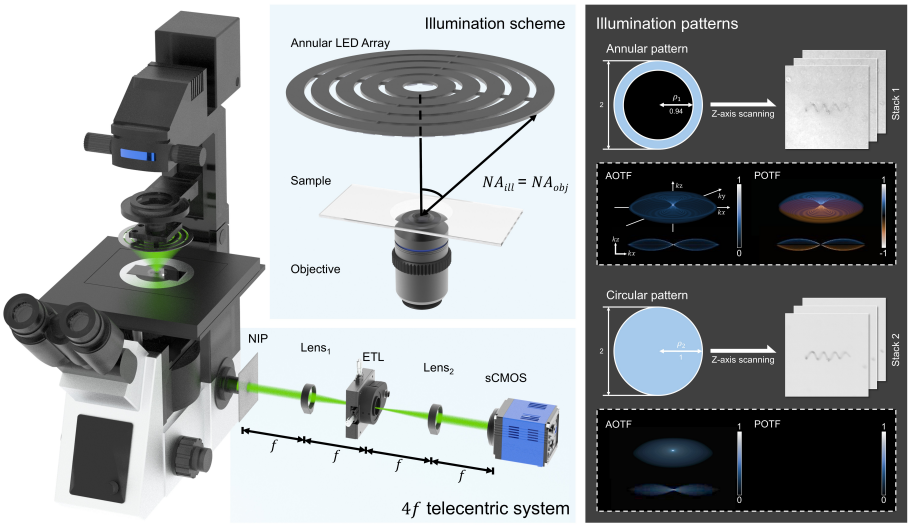

Fig. 1. Diagram of the overall system layout and used illumination apertures. Left: The scheme of the system illustrates the main optical components of the system and their placement (see Visualization 1). Right: 3D OTF rendering and slicing results corresponding to the applied annular and circular apertures.

Biomedical Optics EXPRESS

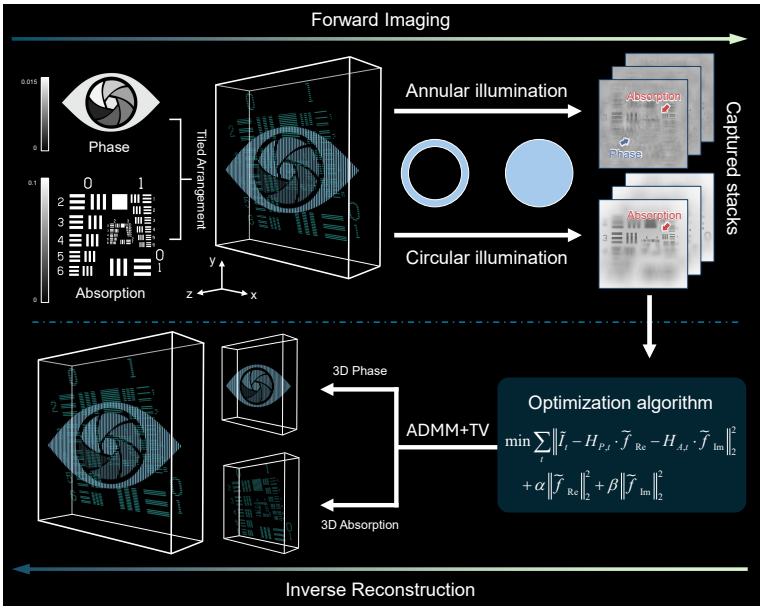

Fig. 2. Forward imaging process and inverse reconstruction pipeline for MM-TIDT method. A 3D complex object is composed of tiled absorption and phase target. Two intensity stacks under different illuminations are captured. The inverse reconstruction algorithm is used for 3D phase and absorption information reconstruction.

sample plane, as shown in Fig. 1. At the original imaging plane of the microscope, an electrically tunable lens (Optotune EL-16-40-TC) is incorporated to create a $4f$ telecentric imaging system for phase modulation. Images are captured using an sCMOS camera (PCO.Edge 4.2) with a pixel resolution of 2048×2048 and a pixel size of 6.5 µm. For label-free imaging, two illumination aperture are used: a circular aperture matching the NA of the objective ($\rho = \rho_p$) and an annular aperture where the outer radius matches the objective's NA ($0.94\,\rho_p \le \rho \le \rho_p$).

Considering the Fourier transform property of the 4f system, the variation of ETL's focal power located at the Fourier plane is equivalent to adding a quadratic phase modulation:

$$t_l(\mu, \xi) = \exp\left[-\frac{i\pi}{\lambda f_{eff}}\left(\mu^2 + \xi^2\right)\right] \tag{8}$$

where (μ, ξ) is the spatial coordinates in the Fourier plane of the 4f system, f_{eff} is the effective focal length of ETL controlled by current. From the angular spectrum perspective, the free-space propagation distance Δz of the wavefield is given by [44] (See Supplement 1 S2 for details):

$$\Delta z = -\frac{1}{M^2}\frac{n \cdot f^2}{f_{eff}} \tag{9}$$

where M is the magnification of the objective lens, n is the refractive index of the immersion medium, and f is the focal length of two Fourier lenses. Since f_{eff} can be electronically controlled, the defocus distance Δz can be easily adjusted.

Furthermore, it should be noted that the precise alignment of the ETL is critical and therefore it is mounted on a translator. The accurate position of the ETL along the optical axis ensures the magnification and lateral shift to be invariant independent of the focal power of ETL. Considering allowable misalignment, we should make pre-calibration of the imaging system, which has been done in our previous work [31].

Biomedical Optics EXPRESS

2.4. Overview of MM-TIDT Method

We constructed a complex 3D object as shown in Fig. 2, and the tilted absorption target and phase target intersect in 3D space. To evaluate the phase and absorption effects separately, we consider the real and imaginary parts of the scattering potential according to Eq. (2) and get two intensity stacks under partially coherent annular illumination and incoherent circular illumination respectively. Then, the iterative ADMM algorithm combined with TV regularization and non-negativity constraint according to Eq. (6) is used for 3D phase and absorption decoupling.

3. Results

3.1. Simulation and experimental results for standard fluorescent polystyrene microspheres

The imaging performance of the method can be validated using fluorescent polystyrene microspheres (Thermo Fisher Scientific Invitrogen TetraSpeck™ Microspheres). In the experiment, fluorescent polystyrene microspheres with a diameter of 4 μm were placed in a liquid medium with a refractive index of 1.63 and stained with green fluorescent dye (maximum excitation/emission wavelengths of 505 nm/515 nm). Two sets of image stacks, each of size 256×256×156 with a

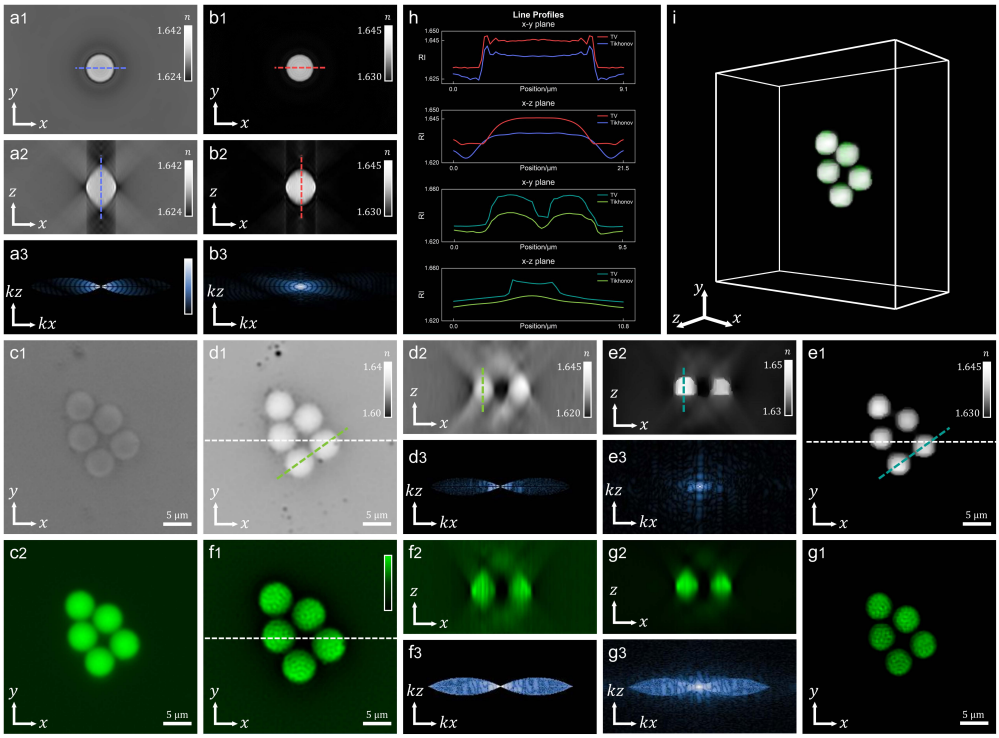

Fig. 3. Results of the fluorescent polystyrene microsphere. **a, b** Comparison of reconstructions of the simulated polystyrene microspheres using Tikhonov regularization versus TV regularization. **c** Cross-sectional *x*-*y* images of actual polystyrene microspheres captured under annular illumination (**c1**) and fluorescence excitation (**c2**). **d, e** Comparison of reconstructions of the actual polystyrene microspheres using Tikhonov regularization versus TV regularization. **f, g** Comparison of reconstructions of the fluorescence stack of the actual polystyrene microspheres using Tikhonov regularization versus TV regularization. **h** Refractive index profiles along the corresponding color lines in **a**, **b**, **d**, and **e**. **i** 3D multi-modal fusion rendering of the reconstructed polystyrene microspheres (see Visualization 2).

Biomedical Optics EXPRESS

volume size of 41.6×41.6×39 μm^3, were captured using two different illumination apertures at an equivalent z-step of 0.25 μm. Additionally, an identical stack was acquired using the fluorescence imaging light path of the microscope. Notably, we first simulated a weakly scattering microsphere sample resembling the polystyrene microspheres, assuming a refractive index of $n_r = 1.645$, while keeping all other parameters consistent with the actual experiment.

In Fig. 3, the comparison between Tikhonov regularization and TV regularization is presented in three sets of results, demonstrating the advantages of our method in noise suppression and detail preservation. Due to the missing cone problem, the reconstructed refractive index values are generally underestimated. However, our approach mitigates the issue of missing spectrum in the reconstruction, as evidenced by Fig. 3(h), where the reconstructed values using our method are closer to the true refractive index values.

3.2. 3D phase and absorption dual-modal imaging results of spirulina specimen

Further more, we demonstrate the system's capability for absorption and phase decoupling by imaging a Spirulina specimen in Fig. 4, which is primarily composed of absorption information. Two sets of image stacks, each of size 1024×1024×121 with a volume size of 166.4×166.4×30.25 μm^3, were captured using two different illumination apertures at an equivalent z-step of 0.25 μm. As seen in Fig. 4(a1) and b1, a2 and b2, the decoupled reconstruction results more accurately describe the structure of Spirulina specimen, and the more complete 3D presentation in Fig. 4(c) also reflects the high-precision 3D reconstruction capability of our method.

3.3. 3D multi-modal imaging results of DAPI labeled C166 cells

Our final experiment demonstrates the 3D multi-modal imaging capabilities of MM-TIDT on DAPI labeled C166 cells in Fig. 5. Two sets of image stacks, each of size 512×512×60 with a volume size of 83.2×83.2×15 μm^3, were captured using two different illumination apertures at an equivalent z-step of 0.25 μm. An identical stack for DAPI was acquired using the fluorescence imaging light path of the microscope. Figures 5(a1)-(a3) shows three x-y slices of different layers of the decoupled absorption information of the cells. Figures 5(b1)-(b3) shows three x-y slices of different layers of the decoupled phase information of the cells. Figures 5(c) shows one layer of

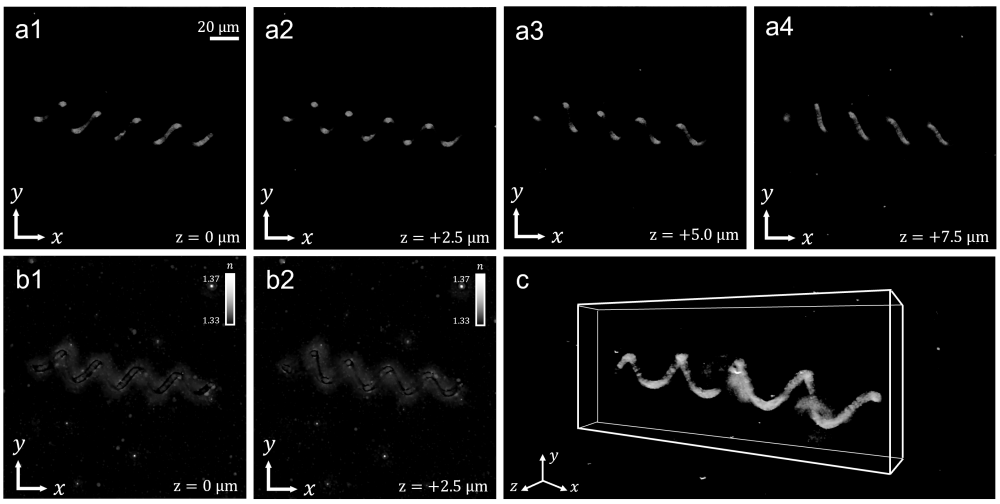

Fig. 4. Results of Spirulina specimen. **a** Absorption results of x-y slices of different layers of the specimen. **b** Phase results of x-y slices of different layers of the specimen. c 3D rendering result of the absorption component of the specimen.

Biomedical Optics EXPRESS

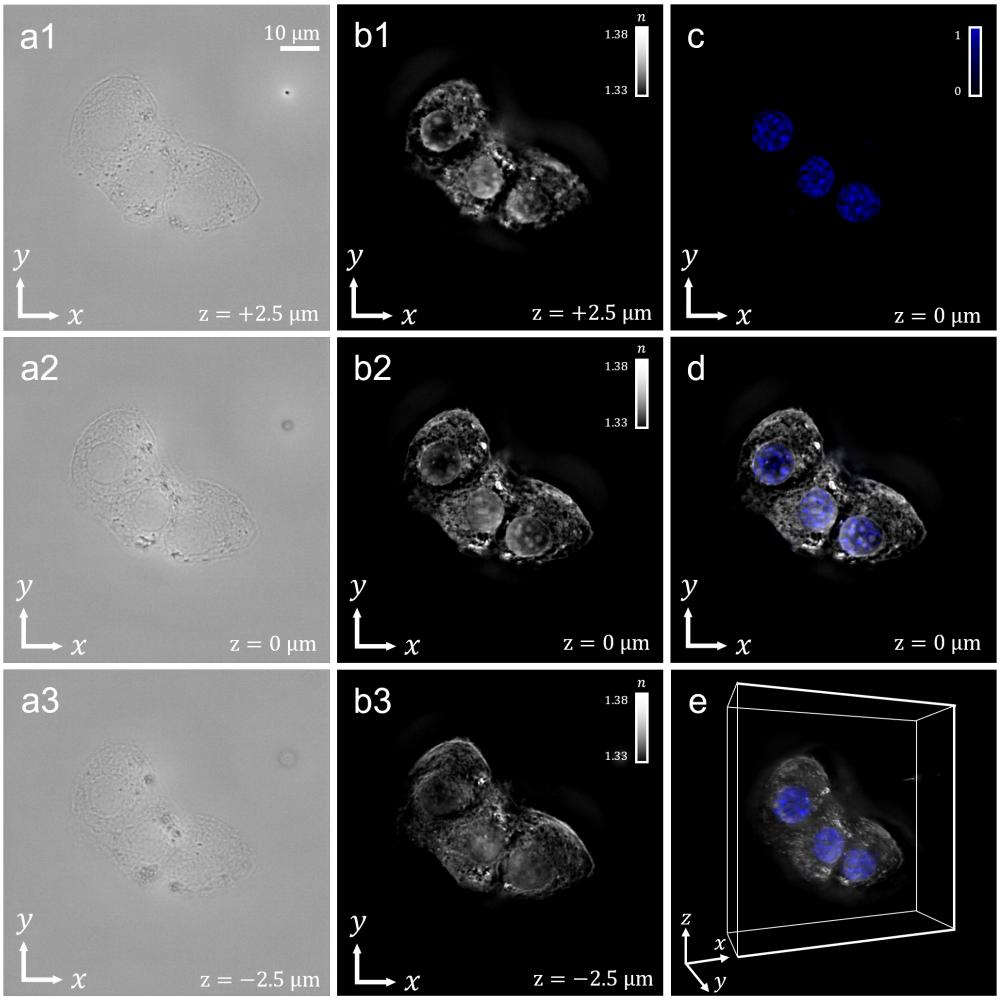

Fig. 5. Results of DAPI labeled C166 cells. **a** Absorption results of x-y slices of different layers of the cell. **b** Phase results of x-y slices of different layers of the cell. **c** Fluorescent result of x-y slice of one layer of the cell. **d** Multi-modal x-y slice for DAPI labeled C166 cells. **e** Multi-modal 3D rendering for DAPI labeled C166 cells.

DAPI labeled nucleus of the C166 cells. The overlay multi-modal information of C166 cells at a certain focal plane is shown in Fig. 5(d). The 3D rendering result of multi-modal reconstruction result of the labeled C166 cells is shown in Fig. 5(e).

4. Conclusion and discussion

In this work, we have demonstrated the decoupling method of the complex refractive index for objects, named MM-TIDT. Employing ADMM TV regularization and non-negative prior, we have demonstrated that the refractive index and absorption components of 3D objects can be resolved from two through-focus intensity stacks. A high-speed ETL located at the Fourier plane of the 4f telecentric module incorporated after the tube lens of the commercial inverted microscope facilitates rapid, programmable, and automated acquisition of a single stack of through-focus intensity images. We first quantitatively verify the effectiveness of MM-TIDT method by standard

Biomedical Optics EXPRESS

fluorescent polystyrene microspheres. Then we demonstrated the capabilities of MM-TIDT by Spirulina algae and C166 cells of which the nuclei were stained with DAPI. Since this technique is compatible with the conventional bright-field microscope (Köhler illumination), and can be easily combined with fluorescence techniques to gain labeled specificity and thus provide a wider window to investigate biological processes [31,37,45,46].

However, some important issues still need to be clarified or require further investigation. First, the theoretical analysis and experimental results suggest that employing intensity stacks with two different illumination patterns is adequate for decoupling 3D absorption and phase information. However, the intricate process of image formation in partially coherent imaging renders the identification of optimal illumination patterns an exceedingly challenging endeavor. The current selection of annular aperture paired with incoherent circular illumination with matched NA is based on empirical criteria that are intuitively linked to the shape of the OTF. The adoption of more sophisticated metrics (merit functions) to evaluate the efficacy of apertures, coupled with the optimization of apertures through advanced algorithms, presents a compelling avenue for future research. Second, although the use of a high-speed ETL instrument has significantly improved the axial acquisition rate by replacing mechanical axial scanning, the current speed is still limited by the performance of the sCMOS camera, as well as the power of the LED light source and the intensity of fluorescence excitation. Currently, at least two stacks are required to achieve decoupling, hence the realization of dynamic experimental observations remains a question worthy of further investigation. This may be further investigated by hardware upgrades (i.e. camera, light source). Third, due to the possible aberrations of the imaging system, the practical OTF may differ from the calculated one. The algorithms for aberrations correction combined with TIDT will result in more accurate imaging reconstruction. Finally, the method we propose conducts reconstruction on weakly scattering objects within the framework of the first-order Born approximation. As a result, its applicability to strongly scattering objects has yet to be validated, a significant area that we intend to explore in our future studies.

Funding. National Natural Science Foundation of China (62227818, 62105151, 62175109, U21B2033); National Key Research and Development Program of China (2022YFA1205002); Leading Technology of Jiangsu Basic Research Plan (BK20192003); Youth Foundation of Jiangsu Province (BK20210338); Biomedical Competition Foundation of Jiangsu Province (BE2022847); Key National Industrial Technology Cooperation Foundation of Jiangsu Province (BZ2022039); Fundamental Research Funds for the Central Universities (30920032101, 30923010206); Fundamental Scientific Research Business Fee Funds for the Central Universities (2023102001); Open Research Fund of Jiangsu Key Laboratory of Spectral Imaging & Intelligent Sense (JSGP202105, JSGP202201).

Disclosures. The authors declare no conflicts of interest.

Data availability. Data underlying the results presented in this paper are not publicly available at this time but may be obtained from the authors upon reasonable request.

Supplemental document. See Supplement 1 for supporting content.

References

1. J. Mertz, "Optical sectioning microscopy with planar or structured illumination," Nat. Methods **8**(10), 811–819 (2011).
2. J. Lippincott-Schwartz, N. Altan-Bonnet, and G. H. Patterson, "Photobleaching and photoactivation: following protein dynamics in living cells," Nat. Cell Biol., 01 Sep 2003, Suppl:S7-14 (2003).
3. J. Pawley, *Handbook of Bological Confocal Microscopy*, 2, 1035–1040 (Springer, 2006).
4. E. Betzig, G. H. Patterson, R. Sougrat, *et al.*, "Imaging intracellular fluorescent proteins at nanometer resolution," Science **313**(5793), 1642–1645 (2006).
5. J. Qian, Y. Cao, Y. Bi, *et al.*, "Structured illumination microscopy based on principal component analysis," eLight **3**(1), 4 (2023).
6. G. Popescu, *Quantitative Phase Imaging of Cells and Tissues* (McGraw-Hill Education, 2011).
7. Y. Park, C. Depeursinge, and G. Popescu, "Quantitative phase imaging in biomedicine," Nat. Photonics **12**(10), 578–589 (2018).
8. C. Zuo, J. Li, J. Sun, *et al.*, "Transport of intensity equation: a tutorial," Optics and Lasers in Engineering **135**, 106187 (2020).
9. T. H. Nguyen, M. E. Kandel, M. Rubessa, *et al.*, "Gradient light interference microscopy for 3d imaging of unlabeled specimens," Nat. Commun. **8**(1), 210 (2017).

Biomedical Optics EXPRESS

10. P. Marquet, B. Rappaz, P. J. Magistretti, *et al.*, "Digital holographic microscopy: a noninvasive contrast imaging technique allowing quantitative visualization of living cells with subwavelength axial accuracy," Opt. Lett. **30**(5), 468–470 (2005).
11. W. Choi, C. Fang-Yen, K. Badizadegan, *et al.*, "Tomographic phase microscopy," Nat. Methods **4**(9), 717–719 (2007).
12. Y. Sung, W. Choi, C. Fang-Yen, *et al.*, "Optical diffraction tomography for high resolution live cell imaging," Opt. Express **17**(1), 266–277 (2009).
13. T. Kim, R. Zhou, M. Mir, *et al.*, "White-light diffraction tomography of unlabelled live cells," Nat. Photonics **8**(3), 256–263 (2014).
14. J. Li, N. Zhou, J. Sun, *et al.*, "Transport of intensity diffraction tomography with non-interferometric synthetic aperture for three-dimensional label-free microscopy," Light:Sci. Appl. **11**(1), 154 (2022).
15. N. Zhou, J. Sun, R. Zhang, *et al.*, "Quasi-isotropic high-resolution fourier ptychographic diffraction tomography with opposite illuminations," ACS Photonics **10**(8), 2461–2466 (2023).
16. N. Zhou, R. Zhang, W. Xu, *et al.*, "High-speed high-resolution transport of intensity diffraction tomography with bi-plane parallel detection," Laser Photonics Reviews **18**(11), 2400387 (2024).
17. J. Rosen, S. Alford, B. Allan, *et al.*, "Roadmap on computational methods in optical imaging and holography," Appl. Phys. B **130**(9), 166 (2024).
18. Z. Huang and L. Cao, "k-space holographic multiplexing for synthetic aperture diffraction tomography," APL Photonics **9**(5), 056101 (2024).
19. Y. Gao and L. Cao, "Motion-resolved, reference-free holographic imaging via spatiotemporally regularized inversion," Optica **11**(1), 32–41 (2024).
20. Y. Baek and Y. Park, "Intensity-based holographic imaging via space-domain Kramers-Kronig relations," Nat. Photonics **15**(5), 354–360 (2021).
21. Y. Cotte, F. Toy, P. Jourdain, *et al.*, "Marker-free phase nanoscopy," Nat. Photonics **7**(2), 113–117 (2013).
22. V. Balasubramani, A. Kuś, H.-Y. Tu, *et al.*, "Holographic tomography: techniques and biomedical applications," Appl. Opt. **60**(10), B65–B80 (2021).
23. R. Horstmeyer, J. Chung, X. Ou, *et al.*, "Diffraction tomography with Fourier ptychography," Optica **3**(8), 827–835 (2016).
24. C. Zuo, J. Sun, J. Li, *et al.*, "Wide-field high-resolution 3d microscopy with fourier ptychographic diffraction tomography," Optics and Lasers in Engineering **128**, 106003 (2020).
25. R. Ling, W. Tahir, H.-Y. Lin, *et al.*, "High-throughput intensity diffraction tomography with a computational microscope," Biomed. Opt. Express **9**(5), 2130–2141 (2018).
26. N. Zhou, J. Li, J. Sun, *et al.*, "Single-exposure 3d label-free microscopy based on color-multiplexed intensity diffraction tomography," Opt. Lett. **47**(4), 969–972 (2022).
27. M. R. Teague, "Deterministic phase retrieval: a Green's function solution," J. Opt. Soc. Am. **73**(11), 1434–1441 (1983).
28. C. Zuo, Q. Chen, W. Qu, *et al.*, "High-speed transport-of-intensity phase microscopy with an electrically tunable lens," Opt. Express **21**(20), 24060–24075 (2013).
29. J. M. Soto, J. A. Rodrigo, and T. Alieva, "Label-free quantitative 3d tomographic imaging for partially coherent light microscopy," Opt. Express **25**(14), 15699–15712 (2017).
30. T. Noda, S. Kawata, and S. Minami, "Three-dimensional phase contrast imaging by an annular illumination microscope," Appl. Opt. **29**(26), 3810–3815 (1990).
31. R. Zhang, N. Zhou, H. Tang, *et al.*, "High-speed multi-modal extended depth-of-field microscopy with an electrically tunable lens," Laser Photonics Reviews **18**(4), 2300770 (2024).
32. M. Chen, L. Tian, and L. Waller, "3d differential phase contrast microscopy," Biomed. Opt. Express **7**(10), 3940–3950 (2016).
33. Z. Bai, Q. Chen, H. Ullah, *et al.*, "Absorption and phase decoupling in transport of intensity diffraction tomography," Optics and Lasers in Engineering **156**, 107082 (2022).
34. S. Boyd, N. Parikh, E. Chu, *et al.*, "Distributed optimization and statistical learning via the alternating direction method of multipliers," Foundations and Trends in Machine learning **3**(1), 1–122 (2010).
35. A. Chambolle, "An algorithm for total variation minimization and applications," Journal of Mathematical Imaging and Vision **20**(1/2), 73–87 (2004).
36. S. Chowdhury, W. J. Eldridge, A. Wax, *et al.*, "Structured illumination microscopy for dual-modality 3d sub-diffraction resolution fluorescence and refractive-index reconstruction," Biomed. Opt. Express **8**(12), 5776–5793 (2017).
37. D. Dong, X. Huang, L. Li, *et al.*, "Super-resolution fluorescence-assisted diffraction computational tomography reveals the three-dimensional landscape of the cellular organelle interactome," Light:Sci. Appl. **9**(1), 11 (2020).
38. E. Wolf, "Three-dimensional structure determination of semi-transparent objects from holographic data," Opt. Commun. **1**(4), 153–156 (1969).
39. A. Devaney, "Inverse-scattering theory within the rytov approximation," Opt. Lett. **6**(8), 374–376 (1981).
40. N. Streibl, "Three-dimensional imaging by a microscope," J. Opt. Soc. Am. A **2**(2), 121–127 (1985).
41. N. Streibl, "Fundamental restrictions for 3-d light distributions," Optik (Stuttgart) **66**, 341–354 (1984).
42. N. Streibl, "Depth transfer by an imaging system," Opt. Acta **31**(11), 1233–1241 (1984).
43. Y. Bao and T. K. Gaylord, "Quantitative phase imaging method based on an analytical nonparaxial partially coherent phase optical transfer function," J. Opt. Soc. Am. A **33**(11), 2125–2136 (2016).

Biomedical Optics EXPRESS

44. J. W. Goodman, *Introduction to Fourier Optics* (Roberts and Company publishers, 2005).
45. Y. Park, G. Popescu, K. Badizadegan, *et al.*, "Diffraction phase and fluorescence microscopy," Opt. Express **14**(18), 8263–8268 (2006).
46. J. Zheng, C. Zuo, P. Gao, *et al.*, "Dual-mode phase and fluorescence imaging with a confocal laser scanning microscope," Opt. Lett. **43**(22), 5689–5692 (2018).